Structural determinants for ligand capture by a class II preQ$_1$ riboswitch

Mijeong Kang[a,b], Catherine D. Eichhorn[a], and Juli Feigon[a,b,1]

[a]Department of Chemistry and Biochemistry and [b]University of California Los Angeles-Department of Energy Institute for Genomics and Proteomics, University of California, Los Angeles, CA 90095

Prequeuosine (preQ$_1$) riboswitches are RNA regulatory elements located in the 5′ UTR of genes involved in the biosynthesis and transport of preQ$_1$, a precursor of the modified base queuosine universally found in four tRNAs. The preQ$_1$ class II (preQ$_1$-II) riboswitch regulates preQ$_1$ biosynthesis at the translational level. We present the solution NMR structure and conformational dynamics of the 59 nucleotide *Streptococcus pneumoniae* preQ$_1$-II riboswitch bound to preQ$_1$. Unlike in the preQ$_1$ class I (preQ$_1$-I) riboswitch, divalent cations are required for high-affinity binding. The solution structure is an unusual H-type pseudoknot featuring a P4 hairpin embedded in loop 3, which forms a three-way junction with the other two stems. ^{13}C relaxation and residual dipolar coupling experiments revealed interhelical flexibility of P4. We found that the P4 helix and flanking adenine residues play crucial and unexpected roles in controlling pseudoknot formation and, in turn, sequestering the Shine–Dalgarno sequence. Aided by divalent cations, P4 is poised to act as a "screw cap" on preQ$_1$ recognition to block ligand exit and stabilize the binding pocket. Comparison of preQ$_1$-I and preQ$_1$-II riboswitch structures reveals that whereas both form H-type pseudoknots and recognize preQ$_1$ using one A, C, or U nucleotide from each of three loops, these nucleotides interact with preQ$_1$ differently, with preQ$_1$ inserting into different grooves. Our studies show that the preQ$_1$-II riboswitch uses an unusual mechanism to harness exquisite control over queuosine metabolism.

Riboswitches are functional noncoding RNA elements often found at the 5′ end of genes that bind to effector molecules, usually metabolites, to attenuate gene expression (1–8). They generally contain two modular elements, an aptamer that binds directly to a cognate ligand, followed by an expression platform that carries out the regulatory function. Ligand binding induces a conformational rearrangement in the aptamer domain, which is transduced to the expression platform, turning gene expression on or off at the transcription or translation level.

Structural studies of diverse riboswitches bound to their cognate ligands have revealed that they have evolved various strategies for high-affinity and specific binding between RNA receptors and ligands. In general, the aptamer domain enfolds the ligand, forming a highly complex 3D conformation using a host of tertiary interactions, including base triples, kink turns, ribose zippers, A-minor motifs, loop–loop interactions, and pseudoknots (9–11). Some riboswitches require divalent cations for ligand binding (9, 12–16), whereas in others divalent cations stabilize the bound state (17–21). Some ligands, including S-adenosyl methionine (22), S-adenosyl homocysteine (22, 23), cyclic di-GMP (24, 25), and prequeuosine (preQ$_1$) (26, 27), have more than one class of riboswitch, with each class adopting a different 3D fold to achieve recognition of the same ligand.

Two classes of riboswitches that bind preQ$_1$, a precursor to queuosine, have been identified (26, 27). Queuosine is a hypermodified guanine found universally at the anticodon wobble position of aspartyl, asparaginyl, histidyl, and tyrosyl tRNA (28) and is required for faithful translation (29–31). PreQ$_1$ is the last free precursor in the queuosine biosynthetic pathway before insertion into the tRNA wobble position (32). Whereas bacteria

synthesize queuosine de novo, eukaryotes do not; rather, they acquire queuosine precursors through their environment. preQ$_1$ class I (preQ$_1$-I) riboswitches can regulate either transcription or translation, whereas class II (preQ$_1$-II) riboswitches can regulate only translation (27). preQ$_1$-I riboswitches have among the smallest known minimal aptamers, at 34 nt (26), but preQ$_1$-II riboswitch aptamers are much larger, at ∼60 nt (27). High-resolution X-ray crystal and solution NMR structures have revealed that preQ$_1$-I aptamers form H-type pseudoknots with two stems and three loops (33–36). Subsequent studies detailing preQ$_1$-I riboswitch dynamics and folding pathway have shown that divalent cations bind loop 1 and stabilize the bound conformation (21, 37).

To date, preQ$_1$-II riboswitches have been found primarily in virulent streptococcal strains, such as *Streptococcus pneumoniae* (*Spn*) (27), a significant pathogen that is one of the leading causes of bacterial meningitis (16, 38), making this riboswitch an excellent candidate for antibacterial therapeutic targeting. An X-ray crystal structure of the *Lactobacillus rhamnosus* (*Lra*) preQ$_1$-II riboswitch aptamer bound to preQ$_1$ was recently determined at 2.3 Å (39), revealing a mode of preQ$_1$ recognition different from that of preQ$_1$-I riboswitches, as predicted by in-line probing and mutagenesis experiments (27). On preQ$_1$ binding, the Shine–Dalgarno region is sequestered in an H-type pseudoknot, confirming the mechanism of translation regulation. An unusual feature of the preQ$_1$-II riboswitch is that it contains an evolutionarily conserved but unusual hairpin insertion (P4) in loop 3 (Fig. 1). The position of P4 is fixed in the crystal structure, but single-molecule FRET studies indicate that it is dynamic (40).

Significance

Riboswitches are structured RNA elements, generally found 5′ to protein-coding regions that control gene expression by binding metabolites or other RNAs. The class II prequeuosine riboswitch (preQ$_1$-II) enfolds preQ$_1$ to form a rare example of a pseudoknot with a conserved hairpin embedded in loop 3. The solution NMR structure and dynamics studies of the preQ$_1$-bound *Streptococcus pneumoniae* preQ$_1$-II riboswitch presented here reveal the key functionality of the embedded hairpin in ligand recognition. We show that this hairpin destabilizes formation of the pseudoknot before ligand capture, thereby preventing premature sequestration of the Shine–Dalgarno region, and blocks ligand exit on capture. Our studies show that the preQ$_1$-II riboswitch uses a previously unknown mechanism to harness exquisite control over queuosine metabolism.
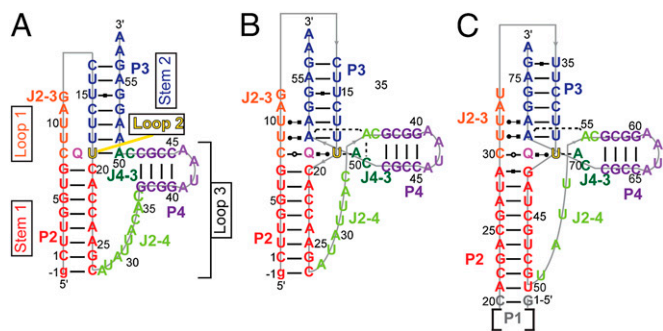

Fig. 1. Secondary structure of preQ$_1$-II riboswitches. (*A*) Predicted secondary structure of the *Spn* riboswitch. Labeling of stems and loops is based on standard H-type pseudoknot nomenclature (73). Numbering of helices (P) and labeling of junction nucleotides (J) is based on ref. 39. (*B*) Determined secondary structure of *Spn*. (*C*) Determined secondary structure of *Lra* (39). Hydrogen bond interactions are shown using the Leontis and Westhof notation (74). The color scheme for structural elements used in this figure is consistent throughout the other figures unless noted otherwise.

Here we present the NMR solution structure of the 59-nt *Spn* preQ$_1$-II riboswitch, one of the largest pseudoknot structures solved by NMR to date. The overall conformation is similar to that of the *Lra* riboswitch, but there are key differences, particularly with respect to the P4 helix orientation. Combining analysis of the structures, ^{13}C R_1 and R_2 relaxation and residual dipolar coupling (RDC) measurements, isothermal calorimetry (ITC), and nucleotide substitutions, we show that the preQ$_1$-II riboswitch uses the accessory hairpin and flanking nucleotides to introduce disorder in the ligand-free state, enabling an open binding pocket to facilitate ligand capture and prevent premature sequestering of the Shine–Dalgarno region. On preQ$_1$ binding, this extended hairpin acts as a screw cap on the binding pocket, blocking ligand exit.

Results and Discussion

preQ$_1$-II Secondary Structure and Cation Dependence of preQ$_1$ Binding.

preQ$_1$-II riboswitches have a predicted secondary structure composed of a small P1 hairpin followed by an H-type pseudoknot containing a hairpin (P4) embedded in loop 3 (Fig. 1*A*). The P1 helix does not contribute to preQ$_1$ binding affinity (27) and was deleted for our structural studies. Otherwise the sequence used is identical to that found in *Spn*, except for an extra G at the 5′ end (Fig. 1*A*). Imino proton spectra of the *Spn* preQ$_1$-II riboswitch in 60 mM KCl showed imino resonances that can be assigned to the P2 and P4 stems (Fig. 2*D*) by analysis of nuclear Overhauser effect spectroscopy (NOESY) spectra (Fig. S1). The binding affinity to preQ$_1$ in 60 mM KCl as measured by ITC was $K_D = 6.5 \pm 0.7$ μM (Fig. 2*A*).

Because previous studies included Mg^{2+} in the buffer (27, 39, 40), we measured the binding affinity in the presence of either Mg^{2+} or Ca^{2+} (Fig. 2 *B* and *C*). The addition of divalent cations Ca^{2+} or Mg^{2+} increased the binding affinity by two orders of magnitude (Fig. 2 *B* and *C*), indicating that divalent cations are required for high-affinity binding of preQ$_1$. The addition of Ca^{2+} (Fig. 2*E*) to the riboswitch in the absence of preQ$_1$ resulted in changes in the imino proton spectra, indicating transient formation of at least the top part of P3. Specifically, imino resonances that can be assigned to the A55-U14, G54-U15, and G53-C16 base pairs of P3 were present in the spectrum, but at reduced intensity compared with resonances from the first six base pairs of P2 (Fig. 2*E*). The addition of preQ$_1$ to the riboswitch with 3 mM Ca^{2+} (15 Ca^{2+} equivalents per RNA) (Fig. 2*F*) resulted in the appearance of several additional imino resonances that can be assigned to the rest of the P3 stem, as well as the imino resonance from preQ$_1$, indicating hydrogen bonding (Fig. 2*F*). The imino resonances of U6 and G7, located

at the top of P2, were shifted significantly, and peak intensities for U14, U15, and G53 in the P3 helix were increased. New imino resonances appeared for U9, U10, U17, U18, forming U9-A51-U18, and U10-A52-U17 base triples, and U19, which base pairs to preQ$_1$. All imino resonances could be assigned to Watson–Crick or Hoogsteen base pairs in the pseudo-heteronuclear correlation spectroscopy (J$_{NN}$-COSY) experiment (Fig. S2) with the exception of U19, indicating that U19 base pairs directly to preQ$_1$. The overall secondary structure and tertiary interactions, as revealed from the structure determination described below, are summarized in Fig. 1*B*.

NMR Solution Structure of the preQ$_1$-Bound preQ$_1$-II Riboswitch from *Spn*.

Although the binding affinity of preQ$_1$ to the preQ$_1$-II riboswitch was similar in the presence of either Mg^{2+} or Ca^{2+}, the NMR spectra of the riboswitch with Ca^{2+} were better resolved (Fig. S3). Thus, the NMR solution structure of the 59-nt *Spn* preQ$_1$-II riboswitch in complex with preQ$_1$ was determined in 60 mM KCl and 3 mM CaCl$_2$, using 866 nuclear Overhauser effect (NOE) restraints and 103 RDCs (Table S1). The large size made NMR structure determination particularly challenging. Superposition of the 18 lowest-energy structures over all nucleotides except dynamic single-stranded residues (i.e., J2-4, the P4 apical loop, and the 3′ overhang A57-A58) gave an rmsd of 1.13 Å (Fig. 3*A*). The riboswitch folded into an H-type pseudoknot with preQ$_1$ at the junction between stems P2 (stem 1) and P3 (stem 2) (Fig. 1*A*).

There are three loops: J2-3 (loop 1), U19 (loop 2), and J2-4 and J4-3 with an intervening P4 hairpin extension (loop 3). The first four J2-3 (loop 1) nucleotides are well ordered and form a continuous helical stack in the major groove adjacent to the 5′ strand of P2. The first of the J2-3 nucleotides, C8, forms a noncanonical pair with the Watson–Crick face of preQ$_1$ at the
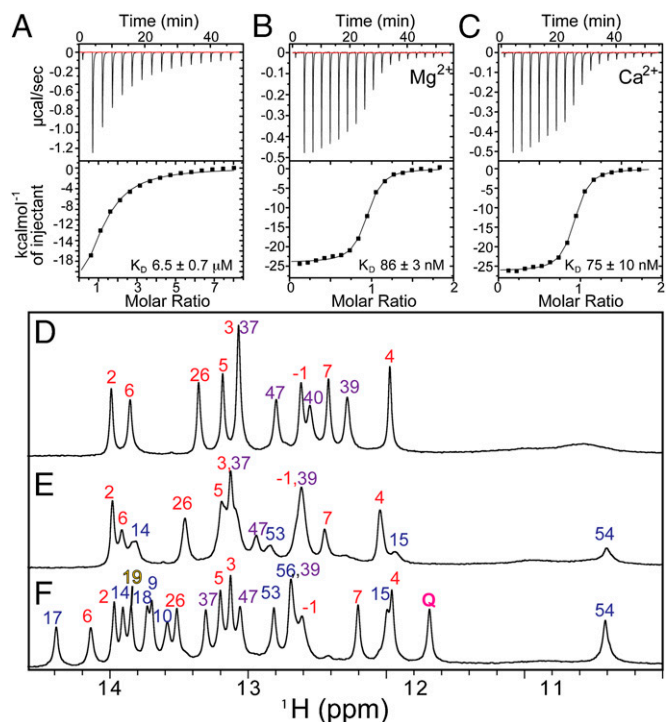

Fig. 2. (*A*–*C*) ITC of preQ$_1$ titration with *Spn* preQ1-II riboswitch at pH 6.3, 25 °C in 60 mM KCl (*A*), 60 mM KCl and 3 mM CaCl$_2$ (*B*), and 60 mM KCl and 3 mM MgCl$_2$ (*C*). (*D*–*F*) One-dimensional imino proton spectra (800-MHz NMR) of 0.2 mM *Spn* preQ$_1$-II riboswitch at pH 6.3, 27 °C in 60 mM KCl (*D*), 60 mM KCl and 3 mM CaCl$_2$ (15 equivalents) (*E*), and 60 mM KCl, 3 mM CaCl$_2$, and 2 equivalents of preQ$_1$ (*F*).
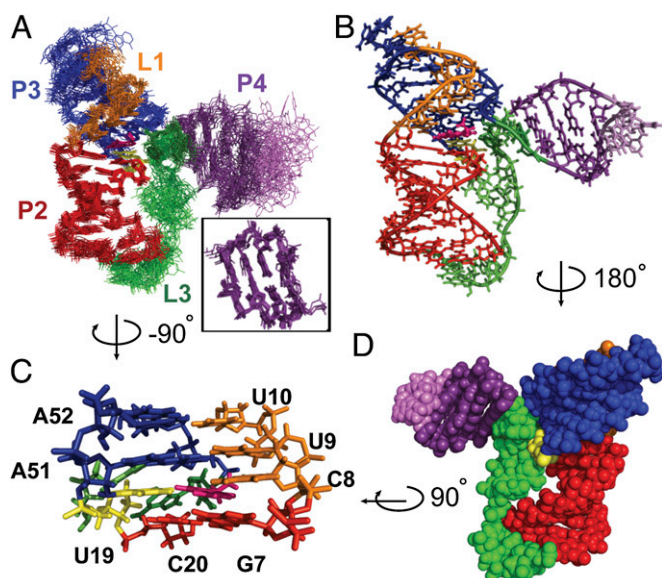
Fig. 3. NMR solution structure of the *Spn* preQ₁-II riboswitch in complex with preQ₁. (*A*) Superposition of the 18 lowest-energy structures. Superposition is on P2, L1, P3, and L2 residues (all heavy atoms). (*Inset*) Superposition of P4 stem residues only. (*B*) Stick representation of the lowest-energy structure. (*C*) Stick representation of the binding pocket with the G-C base pair below and two U-A-U triples above C8-preQ₁-U19-A50, rotated 90° from *B* (side view). (*D*) Sphere representation of the lowest-energy structure, rotated 180° from *B* (back view).

junction between P2 and P3, and the next two nucleotides, U9 and U10, form Hoogsteen base pairs to A51 and A52, respectively, to form U-A-U triples in P3. Together, these residues form a short triple helix at and above the preQ₁ binding pocket (Fig. 3*C*), where the loop 1-stem 2 base pairs stack on stem 1. Triple helices formed between loop 1 and stem 2 at the junction between the two stems of an H-type pseudoknot are a frequent feature in, for example, telomerase pseudoknots (41, 42) and other riboswitches (33–35, 43, 44).

In contrast to J2-3 (loop 1), most of J2-4 is not well structured. J2-4 is also unusual in that these loop 3 nucleotides do not lie along the minor groove, as is the usual case for H-type pseudoknots, but rather extend along one face of P2 across the major groove (Fig. 3*D*). The two J4-3 nucleotides and the last two J2-4

nucleotides stack on P4 to form a structured extension (extended P4) that forms a three-way junction with P2 and P3. The extended P4 hairpin, as well as loop 2 residue U19, block the exit of preQ₁ from the minor groove (Fig. 3 *B* and *D*). P4 is approximately perpendicular to the coaxially stacked P2-P3 module, with a 77° bend angle relative to the helical axis of P2. The P4 helix is well defined by the NMR data (Fig. 3*A*, *Inset*), but its position relative to P2 and P3 is not, owing to conformational dynamics at the junction, as discussed below.

Conformational Dynamics of the preQ₁-Bound Riboswitch. The single-stranded residues in J2-4 and loop 1 are less well defined compared with the rest of the structure. We performed ¹³C R₁ and R₁ρ relaxation experiments to determine whether these regions are inherently flexible. We assessed the level of dynamics at ps to ns timescales by computing $2R_2 - R_1$, which approximates the S^2 degree of order (45), and normalizing to base-paired residues within the P2 stem (S^2_{rel}; Fig. 4) (46, 47). In general, P2 and P3 are ordered with similar S^2_{rel} values, ~1. Loop 1 residues A11 and G12 are moderately dynamic, whereas J2-4 residues U29-C34 are extremely flexible. A35 and A50, at the end of P4 at the three-way junction, are rigid, although the nucleobase C8 bond vector of A50 has a reduced S^2_{rel} of ~0.9. S^2_{rel} values of P4 residues C45–C48, as well as C49, are reduced compared with those of P2 and P3 ($S^2_{rel} \sim 0.9$), suggesting that P4 is dynamic relative to the coaxially stacked P2 and P3 helices. S^2_{rel} values of A57 and A58 are successively lower, indicating that these terminal unpaired residues are flexible.

Whereas R₁ and R₁ρ report on ps-ns dynamics, RDCs have an extended timescale resolution and are sensitive to internal motions ranging from ps to ms, providing insight into dynamics occurring on an ns-μs timescale (48–54). We performed order tensor analysis (55, 56) using the RAMAH program (57) to compute the generalized degree of order (GDO; ϑ) (58) for each helix. Flexible residues, as determined from relaxation experiments, were excluded. The ratio of the degree of order between two helices ($\vartheta_{int} = \vartheta_{II}/\vartheta_I$) reports on the level of interhelical motions, where 0 has maximum dynamics and 1 has minimum dynamics (58). The ϑ_{int} of P3 relative to P2 was 0.96, suggesting that P3 and P2 have minimal interhelical motions; however, the ϑ_{int} of P4 relative to P2 was 0.75, indicating that P4 is dynamic relative to the rigid P2-P3 helical unit. Assuming a cone motional model (51), this corresponds to a 35° cone.

Whereas both ¹³C spin relaxation and RDC measurements showed that P4 is dynamic, the RDCs suggest a greater degree of flexibility compared with relaxation measurements, indicating
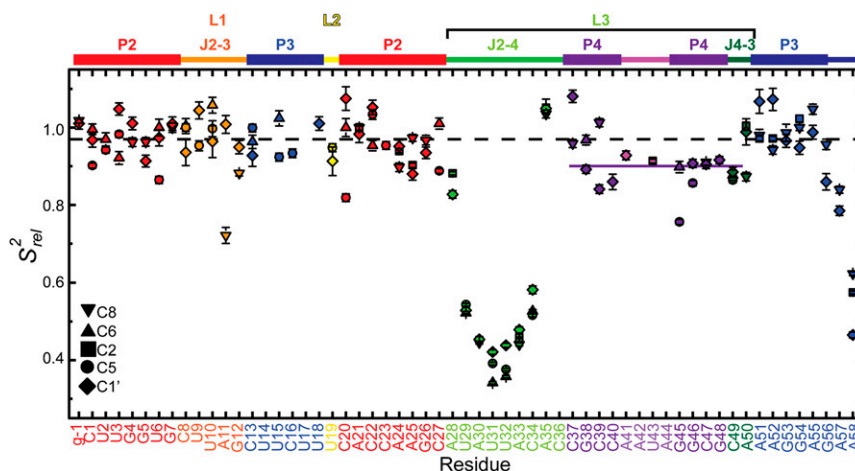

Fig. 4. ¹³C spin relaxation measurements of *Spn* preQ₁-II riboswitch bound to preQ₁. Plot of S^2_{rel} for C8, C6, C2, C5, and C1′ as a function of residue number.

that P4 motions may occur primarily at μs-ms timescales. Independent evidence for the positional dynamics of P4 relative to P2-P3 for *Spn* preQ$_1$ riboswitch was provided by a FRET study in which the observed FRET efficiencies between P3 and P4 suggested that although the P4 helix is near the P3 helix ~50% of the time, the P4 helix spends the rest of the time far from P4 (40).

The preQ$_1$ Binding Pocket. preQ$_1$ binds at the center of the pseudoknot and forms a base quadruple with C8 from loop 1 (J2-3), the single loop 2 nucleotide U19 at the junction between P2 and P3, and A50 from loop 3 (J2-4) (Fig. 5*F*). In the complex, preQ$_1$ forms hydrogen bonds between its "sugar" edge (N2H, N3, and N9H) and the Watson–Crick edge of U19, and forms a *trans* Watson–Crick base pair with the Watson–Crick edge of C8 (O2, N3), with bases positioned such that the preQ$_1$ imino could form a bifurcated hydrogen bond with O2 and N3, whereas the N2H moiety could form a long-range hydrogen bond to the C8 N3 (Fig. 5*F*). The A50 nucleotide rotates over and out of the helix (relative to where it would be if it stacked on P3), such that its sugar is parallel to U19 and its N1 forms a hydrogen bond to the U19 2′OH. The exocyclic methylamine group of preQ$_1$ is positioned such that the amino protons have potential long-range hydrogen bonds with U9 O2 and A51 O2P above (Fig. 5*A*). Below preQ$_1$, the G7-C20 base pair at the top of P2 forms the floor of the binding pocket (Fig. 3*C*). Above preQ$_1$, the U9-A51-U18 triple stacks over the C8-preQ$_1$-U19 triple and A35 N1 hydrogen bonds to A51 2′OH (Fig. 3*C* and Fig. 5 *B* and *E*). Another base triple (U10-A52-U17) stacks above the U9-A51-U18 triple. Thus, the preQ$_1$ binding pocket is stabilized by the triple helix, formed by major groove interactions of J2-3 with preQ$_1$ and P3 and by minor groove interactions of A50 and A35 (Fig. 5 *D–F*). These interactions from the major and minor groove sides, together with the G7-C20 base pair below preQ$_1$, the A51-U18 base pair above, and the loop 2 nucleotide U19 behind, sequester preQ$_1$ in the binding pocket, so that only the exocyclic methylamine group is exposed into the minor groove (Fig. 5*A*).

Dual Role of the Extended P4 Helix in preQ$_1$ Binding. The P4 helix inserted into loop 3 (between J2-4 and J4-3) is an unusual feature of the H-type pseudoknot in this preQ$_1$-II riboswitch. The A35 and A50 nucleotides, which flank C36 and C49 at the ends of P4, are positioned by the P4 helix to rotate A35 above A50 to interact with the U9-A51-U18 triple above the binding pocket. Thus, P4 functions as a "screw cap" to close off the minor groove

side of the binding pocket, opposite J2-3, which closes off the major groove side (Fig. 3*D* and Fig. 5*A*).

To test the importance of the extended P4 helix for preQ$_1$ binding, we made a series of deletions and nucleotide substitutions and investigated the effect on preQ$_1$ binding by ITC (Table S2) and NMR. In the NMR conditions (60 mM KCl, 3 mM CaCl$_2$; pH 6.3), the riboswitch construct used for NMR (WT) has a K_D of 75 ± 10 nM, and the full-length riboswitch including P1 (WT+P1) has a slightly weaker K_D of 220 ± 30 nM. Deletion of residues 36–49 [ΔP4(36-49)], which include all of P4 and the two flanking C residues, from the NMR construct decreased the binding affinity by 20-fold, to 2,000 ± 300 nM. A similar result (K_D = 2,000 nM) was obtained from 2-amino-purine fluorescence measurements on the *Spn* preQ$_1$-II riboswitch with only P4 deleted (equivalent residues 37–48) (40).

Examination of NMR spectra of ΔP4(36-49) showed that deletion of P4 stabilizes P3 base pairs; imino proton resonances for the top five of the six base pairs of P3 were seen in the absence of preQ$_1$ (Fig. S4*B*), whereas in the WT construct only A55-U14, G54-U15, and G53-C16 base pairs were observed (Fig. 2*E* and Fig. S4*A*). However, there was no evidence of the tertiary interactions between loop 1 and P3 that form the two U-A-U triples seen in the preQ$_1$-bound WT riboswitch (Fig. S4*C*).

Examination of thermodynamic parameters from ITC measurements showed that preQ$_1$ binding to the WT preQ$_1$-II riboswitch is enthalpy-driven, with a large unfavorable entropy (−TΔS) of binding (ΔH = −24 ± 0.8 kcal/mol; −TΔS = 17 ± 3.3 kcal/mol) (Table S2). In contrast, the −TΔS of ΔP4(36-49) was 7.8 ± 2.1 kcal/mol, indicating a smaller entropic penalty on binding and in agreement with NMR experiments showing stable formation of P3.

Taken together, the foregoing data suggest that removing P4 reduces the conformational flexibility of loop 3, increasing the probability of pseudoknot formation. Replacement of P4 with a single G increases the K_D by another twofold, to 4,200 nM (40). We hypothesize that this substitution prevents proper positioning of A35 and A50 in the three-way junction, effectively abolishing the screw cap.

We next performed single point mutations to evaluate the role of A35 and A50 on preQ$_1$ binding. A50 and A35 interact with the successive triples with and above preQ$_1$ that block off its exit from the minor groove side via unusual A-minor interactions similar to class III A-minor motif (57), but with *trans* orientation of the glycosidic bonds (*trans* A-minor class III motif) (Fig. 5*B*).
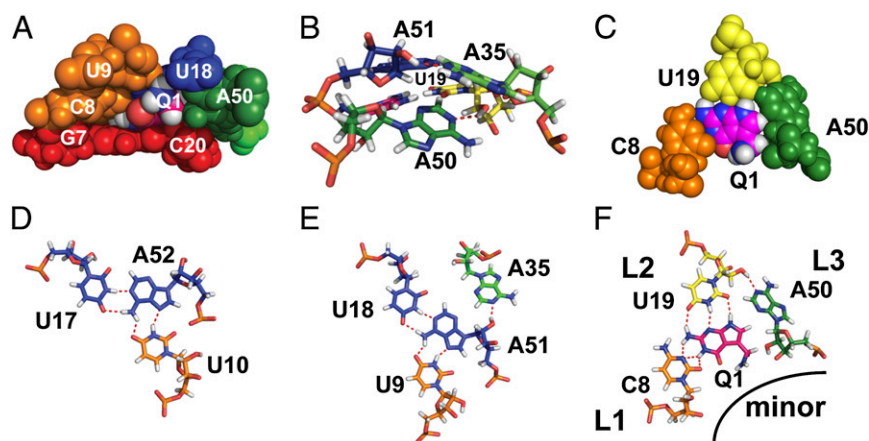

Fig. 5. Structural elements of the preQ$_1$ binding pocket. (*A*) Van der Waals representation of preQ$_1$ in the binding pocket. (*B*) Stick representation showing interactions between A35-A51 and A50-U19, with hydrogen bonds shown as dashed lines (side view). (*C*) Sphere representation of C8-preQ$_1$-U19-A50 interactions, illustrating a van der Waals interaction among A50, U19, and preQ$_1$. (*D–F*) Stick representations of nucleotide interactions in the binding pocket: U10-A52-U17 (*D*), U9-A51-U18-A35 (*E*), and C8-preQ$_1$-U19-A50 (*F*).

Surprisingly, substituting A50 for G resulted in a 280-fold increase in K_D (24 ± 6 μM). The ΔΔG compared with WT was 3.4 kcal/mol, greater than would be expected for the loss of a single hydrogen bond (Table S2). Examination of the position of A50 in the binding pocket revealed that it has almost perfect surface complementarity to preQ₁ and U19 (Fig. 5C), such that A50 provides strong van der Waals interactions. Replacing A50 with G would disrupt not only the single hydrogen bond between A50 N1 and C19 2′OH, but also the van der Waals interactions owing to a steric clash by the G N6 amino group. The van der Waals (or C-H–O) interaction between the preQ₁ exocyclic methylene and A50 2′O might be important in preQ₁ recognition as well (Fig. 5A). In previous studies, ligand analogs that removed the van der Waals interactions (e.g., 7-deazaguanine and guanine) or that added a steric clash (e.g., 7-carboxamide-7-deazaguanine, the carbonyl group of which would clash with A50 2′OH) decreased the binding affinity by more than 100-fold (27). In contrast, dimethylation of the exocyclic amine group, which removes potential hydrogen bonding interactions, decreased binding by only fivefold (27). These findings emphasize the importance of the van der Waals interactions between preQ₁ and J4-3 residue A50 in binding affinity and specific recognition of preQ₁.

A35 N1 hydrogen bonds to A51 2′OH, likely stabilizing the U9-A51-U18 base triple (Fig. 5E). We found that A35G substitution has a smaller (compared with A50G) but nevertheless significant effect on K_D, increasing it to 950 ± 300 nM, consistent with its importance in closing off the minor groove side of the binding pocket. The ΔΔG compared with WT was 1.9 kcal/mol, in the range of the expected cost of losing one hydrogen bond (59). Despite its apparent importance for preQ₁ binding affinity, the reported nucleotide identity for A35 is only 75% conserved (27); however, we noticed that the sequence adjacent to P4 is $A_{33}CA_{35}C$, whereas the shorter J2-4 loop in *Lra* preQ₁-II has only a single AC sequence next to P4 (39). We predicted that deletion of A33 and C34 (ΔA33C34) would not affect preQ₁ binding, and, consistent with this, the NOESY spectra of the imino resonances and the K_D (190 ± 10 nM) were nearly identical to those of WT (Fig. S4 C and D). Substitution of the remaining A35U decreased the binding affinity (K_D = 900 ± 100 nM), with a ΔΔG of 1.5 kcal/mol, indicating that changing A35 to either G or U is equally deleterious. A comparison of the sequences of preQ₁ riboswitches shows that an adenine is always located one to two nucleotides from P4 in the variable length J2-4 (27), suggesting that the reported 75% conservation value may not reflect the true conservation of this residue.

Taken together, the foregoing results indicate that the extended P4 helix serves a dual role in the preQ₁-II riboswitch. In the absence of preQ₁, it reduces the stability of P3, thereby hindering pseudoknot formation, whereas in the presence of preQ₁, the helical twist of P4 places A35 from J2-4 above A50 from J4-3, organizing the three-way junction to cap the minor groove side of the binding pocket. Although neither A35 nor A50 directly hydrogen-bonds to preQ₁, both play significant roles in sequestering preQ₁ in the binding pocket.

Role of Ca²⁺ in Stabilizing the preQ₁ Binding Pocket. Our ITC data indicate that the preQ₁-II riboswitch requires divalent cations for high-affinity preQ₁ binding (Fig. 2 A–C). Although a relatively large unfavorable entropy (17 ± 0.8) kcal/mol of binding preQ₁ was observed for WT in the presence of divalent cations, the −TΔS of binding was significantly larger in the absence of divalent cations (24 ± 3.3 kcal/mol). These data suggest that divalent cations may reduce the inherent conformational entropy in the *Spn* preQ₁-II riboswitch (Table S2). In the presence of preQ₁ without divalent cations, some imino resonances show two peaks, one peak that can be assigned to a ligand-bound state and one peak that can be assigned to a ligand-free state. Surprisingly, even with an excess of preQ₁, the "free" imino resonances do not

disappear, indicating that a population of preQ₁-II riboswitch molecules cannot bind preQ₁ (Fig. S5 A–C).

Although it is unusual that an RNA with weak binding affinity would have ligand binding at slow exchange timescales, this phenomenon has previously been observed in the theophylline riboswitch, which has a small k_{on} value (60). The imino region of the 2D NOESY shows cross-peaks between the two conformers for G4, G7 at the top of P2, and G47 in P4 near the three-way junction, suggesting that the binding pocket is unstable and slowly exchanges between free and bound conformers on timescales ~$1/\tau_m$ (61) in the absence of divalent cations. In addition, no NOE cross-peaks from imino protons of preQ₁, U9, and U10 were detected, indicating that whereas the Watson–Crick base pairs in P3 form A51-U18 and A52-U17, the Hoogsteen base pairs in the base triples at the preQ₁ binding pocket are unstable without divalent cations (Fig. S5 A–C).

When Ca²⁺ was added to the preQ₁-II riboswitch with preQ₁, resonances from several residues near the binding pocket and three-way junction exhibited large chemical shift perturbations, namely A50 C2H2, A35 C2H2 and C1′H1′, U19 C1′H1′, A52 C1′H1′, U18 N3H3, and U17 N3H3 (Fig. 6 and Fig. S5D). The large shifts observed for A35 C2H2 and A50 C2H2 (Fig. 6C) are likely caused by changes in the stacking interactions of A35 and A50 bases as these residues move close to P3, stabilizing the hydrogen bonds from A35 N1 to A51 2′OH and from A50 N1 to U19 2′OH. It is interesting that in the triple helix, the imino chemical shifts from the Watson–Crick paired U17, U18, and U19 are more sensitive to Ca²⁺ than the Hoogsteen paired U9 and U10, likely owing to repositioning of A50 and A35.

Taken together, the foregoing results suggest that in the absence of divalent cations, preQ₁ is able to enter the binding pocket but binds only weakly, with transient formation of base triples containing stable Watson–Crick pairs but unstable Hoogsteen pairs. The addition of Ca²⁺ stabilizes the base triples and A35 and A50 in the binding pocket, allowing high-affinity ligand binding. The *Lra* preQ₁-II riboswitch has two Mg²⁺ ions between J2-4 and P2 (Fig. 7A), which bind near the A35 phosphate backbone (39). We propose that Ca²⁺ is required in the *Spn* preQ₁-II riboswitch for P4 to act as the screw cap by stabilizing the three-way junction.

Comparison with the Crystal Structure of *Lactobacillus rhamnosus* preQ₁-Bound preQ₁-II Riboswitch. The crystal structure of the larger *Lra* preQ₁-II riboswitch, including the P1 hairpin, has been solved to 2.3 Å (Fig. 7A). The structural features of the binding pockets are largely the same, but there are some interesting differences between the solution and crystal structures. In the crystal structure, C30 (equivalent to NMR structure C8) forms a *trans* Watson–Crick/Watson–Crick base pair with preQ₁, whereas in the NMR structure, the preQ₁ imino appears to form a bifurcated hydrogen bond to C8 O2 and N3 (Fig. 5F). No amino resonance was detected for the preQ₁ N2 amino protons, consistent with only a single hydrogen bond forming between the preQ₁ N2 amino and U19 O4 (Fig. S6B). Structure calculations that enforced the hydrogen bonding and planarity seen in C8-preQ₁ base pair in the crystal structure resulted in several NOE violations. Single hydrogen-bonded guanine amino resonances are typically very broad, owing to chemical exchange, and are difficult to detect unless both aminos are hydrogen-bonded. In contrast, for the preQ₁-1 riboswitch, both N2 amino proton resonances, which bind to neighboring residues C19 and A32 (Fig. 7D), were observed in NOESY spectra (Fig. S6A).

In the *Lra* riboswitch, the base pair below the C8-preQ₁ pair, which forms the floor of the binding pocket, is an A-G *cis* Watson–Crick/Watson–Crick base pair, whereas in *Spn*, it is a standard G-C base pair. The A-G base pair increases the C1′–C1′ distance by ~1.5 Å, from 11.2 Å to 12.7 Å, and will have different stacking interactions (62), which may account for the differences in the C8-preQ₁ hydrogen bonds for the two riboswitches.
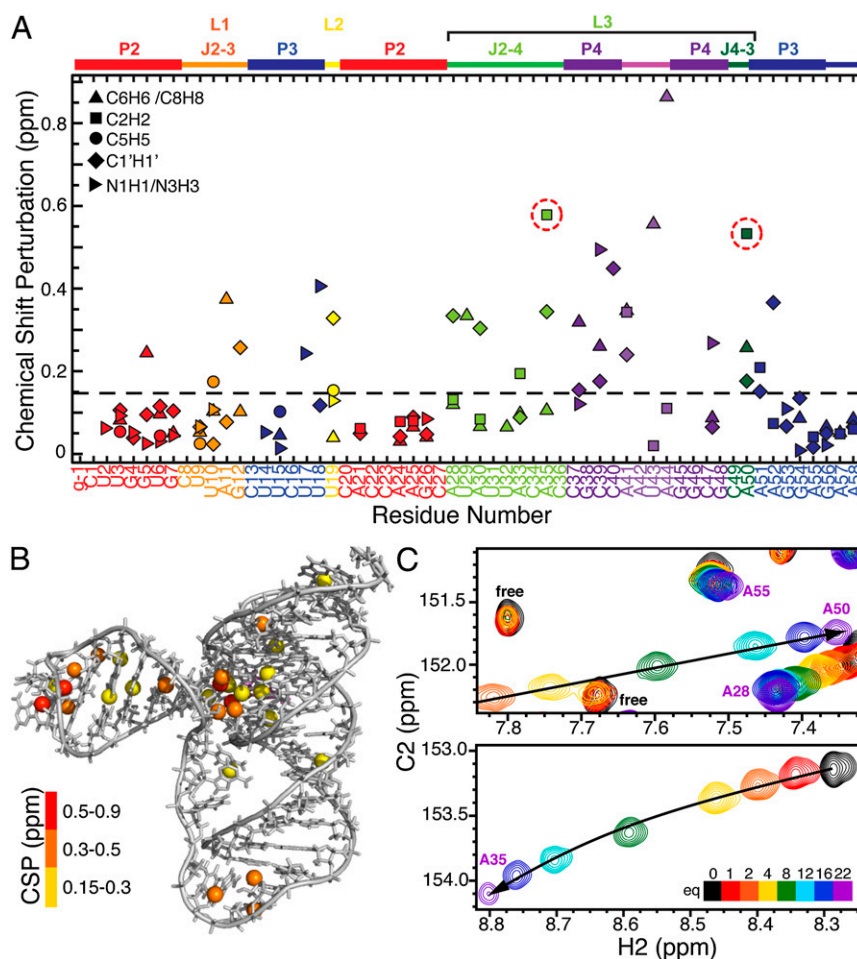
Fig. 6. Ca^{2+} dependence of *Spn* preQ$_1$-II riboswitch. (*A*) Plot of weighted average chemical shift perturbation (CSP) (from 0 to 22 equivalents of Ca^{2+}) of base C-H and N-H and ribose C1'H1' as a function of residue number. Values of A35 and A50 C2H2 are circled. (*B*) CH and NH exhibiting large Ca^{2+}-dependent chemical shifts shown in ball representations in different colors depending on CSP. (*C*) Regions of ^{1}H-^{13}C HSQC spectra of preQ$_1$-II riboswitch as a function of added Ca^{2+} in 60 mM KCl and 2 equivalents of preQ$_1$, pH 6.3, at 27 °C, showing chemical shifts of C2H of A50 (*Upper*) and A35 (*Lower*).

We found a significant difference in the interhelical bend angle between P2 and P4 for *Lra* compared with *Spn* preQ$_1$-II riboswitches (98° vs. 77°). However, our dynamic measurements, as well as previous FRET studies (40), indicate that in solution, P4 samples a range of positions relative to P2-P3, which would include the P2-P4 bend angle of the *Lra* riboswitch. It is possible that the crystallization conditions stabilized the *Lra* riboswitch in this more compact state. Furthermore, there are Cs^+ ions between P4 and J2-4 that could stabilize this bend angle (Fig. 7*A*).

One major sequence difference between the two riboswitches is that the *Lra* riboswitch has a shorter J2-4 (6 nt) and longer P2 (9 bp) than *Spn* (9 nt for J2-4 and 8 bp for P2). The length and sequence of J2-4, which links P2 to P4, is not well conserved evolutionarily, and the effect of J2-4 length on the overall topology and stability of the riboswitch is unclear. Interestingly, divalent cations increase the affinity of the *Lra* preQ$_1$-II riboswitch for preQ$_1$ by only fivefold (39), compared with 200-fold for the *Spn* preQ$_1$-II riboswitch. It is possible that the shorter J2-4 linker in the *Lra* preQ$_1$-II riboswitch may limit the degrees of freedom accessible to loop 3, thereby affecting k_{on} and/or k_{off}.

Comparison of preQ$_1$ Recognition by the preQ$_1$-I and preQ$_1$-II Riboswitches. Structures of transcriptional (*Bacillus subtilis* queC; *Bsu*) (33, 34) and translational (*Thermoanaerobacter tengcongensis*; *Tte*) (35) preQ$_1$-I riboswitches in complex with preQ$_1$ have been

reported previously. Both preQ$_1$-I and preQ$_1$-II riboswitches form H-type pseudoknots when bound to preQ$_1$, and each has interactions along three edges of the preQ$_1$ using one nucleobase each in loop 1, loop 2, and loop 3. However, the arrangement of these three nucleotides differs for the two classes. In both classes of riboswitches, the recognition nucleotides are C, U, and A, but these nucleotides are arrayed around the Watson–Crick, sugar, and imidazole ring edges of the preQ$_1$ differently; for preQ$_1$-II, it is C for loop 1, U for loop 2, and A for loop 3 (Fig. 5*F*), whereas for preQ$_1$-I, it is C for loop 2, A for loop 3, and U for loop 1 (Fig. 7*D*). The three nucleotides also recognize preQ$_1$ differently.

For both classes, the initial or major recognition appears to come from loop 2; however, for preQ$_1$-I, this is a Watson–Crick preQ$_1$-C base pair, whereas for preQ$_1$-II, the loop 2 U binds to the sugar edge of preQ$_1$. For both riboswitches, the exocyclic amino group sticks out into a groove, the minor groove for preQ$_1$-II and the major groove for preQ$_1$-I (Fig. 7*C*). Thus, preQ$_1$ not only is recognized differently by preQ$_1$-I and preQ$_1$-II riboswitches, but also must enter and exit the binding pocket from opposite sides.

These differences in recognition mode can be attributed to the distinct, unusual features of the pseudoknots in the two riboswitch classes. The preQ$_1$-I riboswitches have an unusually long loop 2 (4 nt for *Tte* and 6 nt for *Bsu*) compared with the preQ$_1$-II riboswitches (1 nt), whereas the preQ$_1$-II riboswitches have a G-
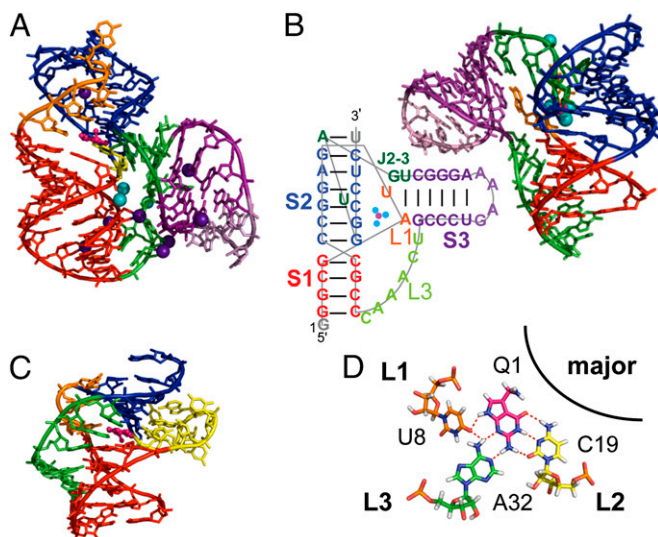
Fig. 7. (*A–C*) Stick representations of *Lra* preQ$_1$-II riboswitch (PDB ID code 4JF2) (*A*), fluoride riboswitch (PDB ID code 4ENC) (*B*), and *Bsu* preQ$_1$-I riboswitch structure (PDB ID code 2L1V) (*C*). (*B, Inset*) Sequence and secondary structure. (*D*) preQ$_1$ base interactions in *Bsu* preQ$_1$-I riboswitch.

C–rich hairpin embedded in loop 3, with single-stranded loop 3 residues traversing the major groove rather than forming A-minor interactions along the minor groove of P2. For these riboswitches to function in gene regulation, it is essential that stem 2 of the pseudoknot (P3) form stably only in the presence of preQ$_1$; otherwise, they will always be in a translationally or transcriptionally off state owing to sequestration of the Shine–Dalgarno sequence or antiterminator, respectively. For the preQ$_1$-II riboswitches, the P4 hairpin helps prevent premature formation of stem 2 (P3) by introducing conformational degrees of freedom, likely aided by the reduced stability of the A-U–rich lower part of P3.

We propose that for preQ$_1$-I riboswitches, the long loop 2 combined with the short unstable stem 2 has the same role. In addition, in contrast to the preQ$_1$-II riboswitches, adding Ca^{2+} to the preQ$_1$-I riboswitches stabilizes preQ$_1$ binding only after preQ$_1$ is in the binding pocket (21). Thus, the two classes of preQ$_1$ riboswitches have evolved different mechanisms to control the switch from hairpin to pseudoknot.

The HL$_{out}$ Pseudoknot Motif. Because an embedded hairpin in pseudoknot loops, classified as HL$_{out}$ type (63), is a rather unusual feature, we searched for other examples with similar topologies. The most similar example is the fluoride riboswitch (Fig. 7*B*), which has a strikingly similar overall fold despite binding a radically different ligand. In this riboswitch, the fluoride ligand coordinates Mg^{2+} ions and binds between P2, P3, and P4 to stabilize the three-way junction, whereas loop 1 and J4-3 form stacking interactions akin to A35 and A50. Another example comes from the glmS ribozyme P3, P4, and P3.1 hairpins, where P4 is the embedded hairpin in loop 3 between P3 (stem 1) and P3.1 (stem 2). Interestingly, the glmS ribozyme P4 hairpin is held rigidly in place in a markedly different orientation than the preQ$_1$-II riboswitch, stabilized by tertiary interactions. The analogous J2-4 linker is limited to 1–4 nt, unlike the preQ$_1$-II riboswitch, which has a longer linker (6–12 nt) (64). Finally, an in vitro evolved aptamer that binds the nerve growth factor protein also has a predicted secondary structure that is highly similar to that of preQ$_1$-II, complete with adenines flanking P4 (65). The topology and mechanism of ligand recognition remain to be elucidated.

Summary

On preQ$_1$ binding to the preQ$_1$-II riboswitch, the Shine–Dalgarno sequence is sequestered within a pseudoknot, thereby preventing translation of preQ$_1$-related mRNAs. To effect proper control of gene expression, the pseudoknot should be formed stably only when the preQ$_1$-II riboswitch captures preQ$_1$. Our NMR structure and dynamics study of the *Spn* preQ$_1$-II riboswitch and comparison with previously solved structures of preQ$_1$-II and preQ$_1$-1 riboswitches have revealed a dual function of the unusual embedded hairpin in loop 3. First, the P4 hairpin introduces conformational disorder to prevent premature pseudoknot formation; then, on preQ$_1$ binding, the extended P4 helix, aided by divalent cations, acts as a screw cap, positioning A35 and A50 to block the exit of preQ$_1$ while also stabilizing the triple helix. PreQ$_1$ is enveloped in the binding pocket, with only its exocyclic methylamine group exposed in the minor groove. Previous structural studies of riboswitches have emphasized the importance of hydrogen bonding and stacking interactions for high specificity and affinity of binding. Here we find that van der Waals interactions between preQ$_1$ and A50 at the end of the extended P4 helix are equally or even more important. In addition, unlike all other purine riboswitches, including preQ$_1$-I, the primary hydrogen-bonding residue forms not a Watson–Crick pair, but rather a noncanonical pair. Finally, to our knowledge, every pseudoknot structure reported to date has loop 3 traversing the minor groove of stem 1; in contrast, in the preQ$_1$-II riboswitch, loop 3 crosses the major groove. This structure provides another example of the diverse ways in which pseudoknots can regulate gene expression and how they can interact with the same ligand in different ways.

Materials and Methods

NMR Sample Preparation. preQ$_1$ was synthesized as described previously (33) and was dissolved in filtered (0.2-μM filter; Nalgen) nanopure water to make a 50 mM stock solution. Unlabeled, base-specifically and uniformly ^{13}C,^{15}N-labeled, and partially deuterated (deuterated at the ribose- 3′, 4′, 5′, 5″ positions of all A, U, G, and C and the 5 position of pyrimidines; Cambridge Isotope Laboratories) *Spn* preQ$_1$-II riboswitch WT and mutant samples were prepared by in vitro transcription using T7 polymerase (P266L mutant) with synthetic DNA templates and purified by denaturing polyacrylamide gel electrophoresis. RNA was eluted from the sliced gel pieces using an Elutrap apparatus (Whatman), and the collected solution was further purified by anion-exchange chromatography (HiTrap DEAE FF; GE Healthcare). The RNA was desalted and concentrated by four washes with filtered nanopure water using Amicon ultrafiltration (Millipore) and then stored at −20 °C. Two equivalents of preQ$_1$ in 50 mM stock solution and 10–20 equivalents of CaCl$_2$ in 1 M stock solution were added to an 0.1–0.2 mM RNA sample in 50 mM KCl (pH 6.3–6.5), after which the volume was reduced to make preQ$_1$-bound RNA NMR samples (0.2 ~1 mM of RNA) using Amicon ultrafiltration (Millipore). NMR samples were prepared in 90% H$_2$O:10% D$_2$O by adding 10% D$_2$O to samples prepared as described above or in D$_2$O by lyophilizing the sample and redissolving in 99.996% D$_2$O (Sigma-Aldrich) several times. For single-bond C-H and N-H RDC measurements, 11 mg/mL Pf1 phage (ASLA Biotech) was added to the ^{13}C,^{15}N-labeled RNA sample in 60 mM KCl and 3 mM CaCl$_2$ (15 equivalents) at pH 6.3.

NMR Spectroscopy and Structure Calculations. NMR spectra were recorded on a Bruker DRX or an Avance 500-, 600-, or 800-MHz spectrometer equipped with an HCN cryogenic probe at 300 K. For the peak assignments, exchangeable proton spectra obtained in 90% H$_2$O/10% D$_2$O and nonexchangeable proton spectra obtained in 99.996% D$_2$O (Sigma-Aldrich) were processed and analyzed using XwinNMR 3.5, Topspin 2.1 (Bruker), and Sparky 3.110 (University of California San Francisco) software. The imino and amino exchangeable protons were assigned from 2D NOESY, 2D ^{1}H-^{15}N HMQC, and 2D H5(C5C4N)H spectra (66, 67). The standard H1′-base proton sequential assignments were initially obtained from analysis of a 2D NOESY experiment with partially deuterated RNA samples and a 2D total correlation spectroscopy (TOCSY) experiment with unlabeled RNA samples. The assignments for all nonexchangeable protons were achieved from analysis of a 2D NOESY experiment of unlabeled RNA samples and 3D HCCH-TOCSY (68) of base-specifically ^{13}C,^{15}N-labeled RNA samples. A suite of 2D-filtered/

edited labeled proton NOESY (F2f, F1fF2e, F1fF2f, and F1eF2e) experiments on base-specifically ^{13}C,^{15}N-labeled RNA samples were used to resolve ambiguous assignments in overlapped regions (69). The assignments of preQ$_1$ and interactions in the binding pocket were identified as described previously (33). Single-bond C-H and N-H RDCs were measured using 2D ^{1}H-^{13}C S3CT-HSQC and standard ^{1}H-^{15}N HSQC experiments as described previously (70), and are listed in Table S3.

Two hundred initial structures of preQ$_1$ riboswitch bound to preQ$_1$ were calculated using Xplor-NIH 2.9.8 starting from an extended, unfolded RNA oligomer using NOE distance and dihedral angle restraints, quantified as described previously (33, 41, 42), following standard Xplor protocols. The 100 lowest-energy structures were further refined. A total of 103 single-bond C-H and N-H RDCs ($^1D_{C1'H1'}$, $^1D_{C8H8}$, $^1D_{C6H6}$, $^1D_{C5H5}$, and $^1D_{C2H2}$; $^1D_{N3H3}$ and $^1D_{N1H1}$) were included for further refinement for the final structures. Order tensor analysis was performed using RAMAH (57), with the lowest-energy NOE-refined solution structure was used as input coordinates. The residues at the end of helices (−1, 27, 57, 58) or determined to be flexible from relaxation experiments (Fig. 4) were excluded from the order tensor analysis. The ϑ_{int} of P3 relative to P2 was close to 1 (0.96), so P2 and P3 were considered one unit with a single order tensor. The ϑ_{int} for P4 relative to P2-P3 was 0.75, and the angle for cone motion (Ψ) of P4 was estimated as 35° [$\vartheta_{int} = 0.5\cos(Y) (1+\cos(Y)$].

A series of grid searches were performed to identify the optimal D$_a$ and D$_r$ values, and the lowest-energy structures were obtained with D$_a$ = −17.85 and D$_r$ = 0.65 for P2-P3, and D$_a$ = −14.82 and D$_r$ = 0.49 for P4. For structure refinement with RDCs, all RDCs except those from J2-4 (28–34) and the P4 loop (41–44) were used. Experimental restraints and structural statistics for the 18 lowest-energy structures are given in Table S1. All structures were viewed and analyzed with MOLMOL (71) and PyMOL (DeLano Scientific). The overall axis bend of P4 relative to the axis of P2 was obtained using Curves 5.3 (72).

^{13}C Spin Relaxation.

Longitudinal (R$_1$) and rotating-frame (R$_{1\rho}$) relaxation rates were measured for C2, C6, C8, C5, and C1' using transverse relaxation optimized spectroscopy (TROSY)-detected pulse sequences (47). Uniformly and base-specifically (A,U and G,C) ^{13}C,^{15}N-labeled preQ$_1$ riboswitches bound to preQ$_1$ samples in D$_2$O were used for relaxation experiments. The carbon carrier was centered at 146 ppm for C8 of the ^{13}C,^{15}N-A,U–labeled samples; at 137 ppm for C8 of the ^{13}C,^{15}N-G,C–labeled samples; and at 88 ppm for C1' and at 99 ppm for C5 of both the ^{13}C,^{15}N-A,U– and ^{13}C,^{15}N-G,C–labeled samples. The spin-lock offsets were 1,700 Hz for C8 of the ^{13}C,^{15}N-A, U–labeled samples; 2,750 Hz for C8 of the ^{13}C,^{15}N-G,C–labeled samples; 2,000

Hz for C1' and −2,000 Hz for C5 of the ^{13}C,^{15}N-G,C–labeled samples; and −1,750 Hz for C5 of the ^{13}C,^{15}N-A,U–labeled samples (47). Relaxation delays were 20 and 540 (×2) ms for C8 and C5 and 20 and 800 (×2) for C1' R$_1$ experiments, and 4, 16 (×2), 24 (×2), and 28 ms for C8; 4, 16, 24, and 28 (×2) ms for C5; and 4, 16, 24 (×2), and 28 ms for C1' R$_{1\rho}$ experiments. (Here ×2 indicates duplicated measurements.) The intensities of each peak were measured using NMRView, and relaxation rates were obtained by fitting the intensities to a monoexponential decay, $I_t = I_0 e^{-Rxt}$ (45), using in-house software. The calibrated high-power off-resonance spin-lock power on the 600-MHz spectrometer (ν_{SL} = 4,208 Hz) was used (21). The transverse relaxation rates (R$_2$) were calculated from R$_1$ and R$_{1\rho}$ rates using R$_{1\rho}$ = R$_1\cos^2\theta$ + R$_2\sin^2\theta$, where $\theta = \arctan(\nu_{SL}/\Omega)$ is the effective tilt angle in the spin-lock field and Ω is the resonance offset from the spin-lock carrier frequency (in Hz). R$_1$ and R$_2$ rates are listed in Table S4.

Ca^{2+} Titration Experiments.

Two-dimensional ^{1}H-^{13}C HSQC experiments were run on the 0.5 mM ^{13}C,^{15}N-A–labeled and ^{13}C,^{15}N-G–labeled preQ$_1$ riboswitch bound to preQ$_1$ in 60 mM KCl with increasing Ca^{2+} concentration from 0 to 40 equivalents of CaCl$_2$. CaCl$_2$ from a 1 M stock solution was added to the NMR sample. Weighted chemical shift perturbation data were calculated using the equation $\Delta = \sqrt{(\Delta\delta_H)^2 + (0.25\Delta\delta_C)^2}$, where ΔH and ΔC are chemical shift differences in the proton dimension and carbon dimension, respectively (61).

ITC Titration.

Binding of WT and mutant preQ$_1$-II riboswitches was measured by ITC using a MicroCal iTC200 device (GE Healthcare). RNA stock solutions in water, prepared as described above, were lyophilized and redissolved in ITC buffer solution [10 mM KPO$_4$ (pH 6.3), 60 mM KCl, 3 mM CaCl$_2$] to a concentration of 10–50 μM RNA. preQ$_1$ was dissolved in the ITC buffer to 100–500 μM. The preQ$_1$ solution was titrated into the RNA samples at 25 °C. Each ITC experiment except for ΔA33C34 was performed in at least duplicate. Calorimetric data were analyzed with Origin 7.0 software.

1. Montange RK, Batey RT (2008) Riboswitches: Emerging themes in RNA structure and function. *Annu Rev Biophys* 37:117–133.
2. Coppins RL, Hall KB, Groisman EA (2007) The intricate world of riboswitches. *Curr Opin Microbiol* 10(2):176–181.
3. Edwards TE, Klein DJ, Ferré-D'Amaré AR (2007) Riboswitches: Small-molecule recognition by gene regulatory RNAs. *Curr Opin Struct Biol* 17(3):273–279.
4. Tucker BJ, Breaker RR (2005) Riboswitches as versatile gene control elements. *Curr Opin Struct Biol* 15(3):342–348.
5. Barrick JE, Breaker RR (2007) The distributions, mechanisms, and structures of metabolite-binding riboswitches. *Genome Biol* 8(11):R239.
6. Mandal M, Breaker RR (2004) Gene regulation by riboswitches. *Nat Rev Mol Cell Biol* 5(6):451–463.
7. Breaker RR (2008) Complex riboswitches. *Science* 319(5871):1795–1797.
8. Serganov A, Nudler E (2013) A decade of riboswitches. *Cell* 152(1-2):17–24.
9. Dann CE, 3rd, et al. (2007) Structure and mechanism of a metal-sensing regulatory RNA. *Cell* 130(5):878–892.
10. Garst AD, Batey RT (2009) A switch in time: Detailing the life of a riboswitch. *Biochim Biophys Acta* 1789(9-10):584–591.
11. Appasamy SD, Ramlan EI, Firdaus-Raih M (2013) Comparative sequence and structure analysis reveals the conservation and diversity of nucleotide positions and their associated tertiary interactions in the riboswitches. *PLoS ONE* 8(9):e73984.
12. Cromie MJ, Shi Y, Latifi T, Groisman EA (2006) An RNA sensor for intracellular Mg(2+). *Cell* 125(1):71–84.
13. Serganov A (2010) Determination of riboswitch structures: Light at the end of the tunnel? *RNA Biol* 7(1):98–103.
14. Pikovskaya O, Serganov AA, Polonskaia A, Serganov A, Patel DJ (2009) Preparation and crystallization of riboswitch-ligand complexes. *Methods Mol Biol* 540:115–128.
15. Kulshina N, Baird NJ, Ferré-D'Amaré AR (2009) Recognition of the bacterial second messenger cyclic diguanylate by its cognate riboswitch. *Nat Struct Mol Biol* 16(12):1212–1217.
16. Barichello T, Generoso JS, Collodel A, Moreira AP, Almeida SM (2012) Pathophysiology of acute meningitis caused by *Streptococcus pneumoniae* and adjunctive therapy approaches. *Arq Neuropsiquiatr* 70(5):366–372.
17. Cochrane JC, Lipchock SV, Strobel SA (2007) Structural investigation of the GlmS ribozyme bound to its catalytic cofactor. *Chem Biol* 14(1):97–105.
18. Buck J, Noeske J, Wöhnert J, Schwalbe H (2010) Dissecting the influence of Mg2+ on 3D architecture and ligand-binding of the guanine-sensing riboswitch aptamer domain. *Nucleic Acids Res* 38(12):4143–4153.
19. Noeske J, Schwalbe H, Wöhnert J (2007) Metal-ion binding and metal-ion induced folding of the adenine-sensing riboswitch aptamer domain. *Nucleic Acids Res* 35(15):5262–5273.
20. Hennelly SP, Novikova IV, Sanbonmatsu KY (2013) The expression platform and the aptamer: Cooperativity between Mg2+ and ligand in the SAM-I riboswitch. *Nucleic Acids Res* 41(3):1922–1935.
21. Zhang Q, Kang M, Peterson RD, Feigon J (2011) Comparison of solution and crystal structures of preQ1 riboswitch reveals calcium-induced changes in conformation and dynamics. *J Am Chem Soc* 133(14):5190–5193.
22. Batey RT (2011) Recognition of S-adenosylmethionine by riboswitches. *Wiley Interdiscip Rev RNA* 2(2):299–311.
23. Wang JX, Breaker RR (2008) Riboswitches that sense S-adenosylmethionine and S-adenosylhomocysteine. *Biochem Cell Biol* 86(2):157–168.
24. Sudarsan N, et al. (2008) Riboswitches in eubacteria sense the second messenger cyclic di-GMP. *Science* 321(5887):411–413.
25. Lee ER, Baker JL, Weinberg Z, Sudarsan N, Breaker RR (2010) An allosteric self-splicing ribozyme triggered by a bacterial second messenger. *Science* 329(5993):845–848.
26. Roth A, et al. (2007) A riboswitch selective for the queuosine precursor preQ1 contains an unusually small aptamer domain. *Nat Struct Mol Biol* 14(4):308–317.
27. Meyer MM, Roth A, Chervin SM, Garcia GA, Breaker RR (2008) Confirmation of a second natural preQ1 aptamer class in Streptococcaceae bacteria. *RNA* 14(4):685–695.
28. Harada F, Nishimura S (1972) Possible anticodon sequences of tRNA His, tRNA Asm, and tRNA Asp from *Escherichia coli* B: Universal presence of nucleoside Q in the first postion of the anticondons of these transfer ribonucleic acids. *Biochemistry* 11(2):301–308.
29. Bienz M, et al. (1981) Usage of the three termination codons in a single eukaryotic cell, the *Xenopus laevis* oocyte. *Nucleic Acids Res* 9(15):3835–3850.
30. Meier F, Suter B, Grosjean H, Keith G, Kubli E (1985) Queuosine modification of the wobble base in tRNAHis influences "in vivo" decoding properties. *EMBO J* 4(3):823–827.

31. Urbonavicius J, Qian Q, Durand JM, Hagervall TG, Björk GR (2001) Improvement of reading frame maintenance is a common function for several tRNA modifications. *EMBO J* 20(17):4863–4873.

32. Noguchi S, Nishimura Y, Hirota Y, Nishimura S (1982) Isolation and characterization of an *Escherichia coli* mutant lacking tRNA-guanine transglycosylase: Function and biosynthesis of queuosine in tRNA. *J Biol Chem* 257(11):6544–6550.

33. Kang M, Peterson R, Feigon J (2009) Structural Insights into riboswitch control of the biosynthesis of queuosine, a modified nucleotide found in the anticodon of tRNA. *Mol Cell* 33(6):784–790.

34. Klein DJ, Edwards TE, Ferré-D'Amaré AR (2009) Cocrystal structure of a class I preQ1 riboswitch reveals a pseudoknot recognizing an essential hypermodified nucleobase. *Nat Struct Mol Biol* 16(3):343–344.

35. Jenkins JL, Krucinska J, McCarty RM, Bandarian V, Wedekind JE (2011) Comparison of a preQ1 riboswitch aptamer in metabolite-bound and free states with implications for gene regulation. *J Biol Chem* 286(28):24626–24637.

36. Spitale RC, Torelli AT, Krucinska J, Bandarian V, Wedekind JE (2009) The structural basis for recognition of the PreQ0 metabolite by an unusually small riboswitch aptamer domain. *J Biol Chem* 284(17):11012–11016.

37. Suddala KC, et al. (2013) Single transcriptional and translational preQ1 riboswitches adopt similar pre-folded ensembles that follow distinct folding pathways into the same ligand-bound structure. *Nucleic Acids Res* 41(22):10462–10475.

38. van de Beek D, et al. (2004) Clinical features and prognostic factors in adults with bacterial meningitis. *N Engl J Med* 351(18):1849–1859.

39. Liberman JA, Salim M, Krucinska J, Wedekind JE (2013) Structure of a class II preQ1 riboswitch reveals ligand recognition by a new fold. *Nat Chem Biol* 9(6):353–355.

40. Soulière MF, et al. (2013) Tuning a riboswitch response through structural extension of a pseudoknot. *Proc Natl Acad Sci USA* 110(35):E3256–E3264.

41. Theimer CA, Blois CA, Feigon J (2005) Structure of the human telomerase RNA pseudoknot reveals conserved tertiary interactions essential for function. *Mol Cell* 17(5):671–682.

42. Cash DD, et al. (2013) Pyrimidine motif triple helix in the *Kluyveromyces lactis* telomerase RNA pseudoknot is essential for function in vivo. *Proc Natl Acad Sci USA* 110(27):10970–10975.

43. Ren A, Rajashankar KR, Patel DJ (2012) Fluoride ion encapsulation by Mg2+ ions and phosphates in a fluoride riboswitch. *Nature* 486(7401):85–89.

44. Gilbert SD, Rambo RP, Van Tyne D, Batey RT (2008) Structure of the SAM-II riboswitch bound to S-adenosylmethionine. *Nat Struct Mol Biol* 15(2):177–182.

45. Lipari G, Szabo A (1982) Model-free approach to the interpretation of nuclear magnetic-resonance relaxation in macromolecules, 2: Analysis of experimental results. *J Am Chem Soc* 104(17):4559–4570.

46. Fushman D, Tjandra N, Cowburn D (1999) An approach to direct determination of protein dynamics from N-15 NMR relaxation at multiple fields, independent of variable N-15 chemical shift anisotropy and chemical exchange contributions. *J Am Chem Soc* 121(37):8577–8582.

47. Hansen AL, Al-Hashimi HM (2007) Dynamics of large elongated RNA by NMR carbon relaxation. *J Am Chem Soc* 129(51):16072–16082.

48. Tolman JR, Al-Hashimi HM (2003) NMR studies of biomolecular dynamics and structural plasticity using residual dipolar couplings. *Annual Reports on NMR Spectroscopy* 51:105–166.

49. Getz M, Sun X, Casiano-Negroni A, Zhang Q, Al-Hashimi HM (2007) NMR studies of RNA dynamics and structural plasticity using NMR residual dipolar couplings. *Biopolymers* 86(5-6):384–402.

50. Eichhorn CD, Yang S, Al-Hashimi HM (2012) Characterising RNA dynamics using NMR residual dipolar couplings. *Recent Developments in Biomolecular NMR*, eds Clore GM, Potts J (Royal Society of Chemistry, Cambridge, UK), pp 184–215.

51. Tolman JR, Flanagan JM, Kennedy MA, Prestegard JH (1997) NMR evidence for slow collective motions in cyanometmyoglobin. *Nat Struct Biol* 4(4):292–297.

52. Peti W, Meiler J, Brüschweiler R, Griesinger C (2002) Model-free analysis of protein backbone motion from residual dipolar couplings. *J Am Chem Soc* 124(20):5822–5833.

53. Tolman JR, Ruan K (2006) NMR residual dipolar couplings as probes of biomolecular dynamics. *Chem Rev* 106(5):1720–1736.

54. Bothe JR, et al. (2011) Characterizing RNA dynamics at atomic resolution using solution-state NMR spectroscopy. *Nat Methods* 8(11):919–931.

55. Bailor MH, et al. (2007) Characterizing the relative orientation and dynamics of RNA A-form helices using NMR residual dipolar couplings. *Nat Protoc* 2(6):1536–1546.

56. Losonczi JA, Andrec M, Fischer MW, Prestegard JH (1999) Order matrix analysis of residual dipolar couplings using singular value decomposition. *J Magn Reson* 138(2):334–342.

57. Hansen AL, Al-Hashimi HM (2006) Insight into the CSA tensors of nucleobase carbons in RNA polynucleotides from solution measurements of residual CSA: Towards new long-range orientational constraints. *J Magn Reson* 179(2):299–307.

58. Tolman JR, Al-Hashimi HM, Kay LE, Prestegard JH (2001) Structural and dynamic analysis of residual dipolar coupling data for proteins. *J Am Chem Soc* 123(7):1416–1424.

59. Vendeix FA, Munoz AM, Agris PF (2009) Free energy calculation of modified base-pair formation in explicit solvent: A predictive model. *RNA* 15(12):2278–2287.

60. Latham MP, Zimmermann GR, Pardi A (2009) NMR chemical exchange as a probe for ligand-binding kinetics in a theophylline-binding RNA aptamer. *J Am Chem Soc* 131(14):5052–5053.

61. Cavanagh J, Fairbrother WJ, Palmer AGI, Skelton NJ (1996) *Protein NMR Spectroscopy* (Academic Press, San Diego, CA).

62. Oliva R, Tramontano A, Cavallo L (2007) Mg2+ binding and archaeosine modification stabilize the G15 C48 Levitt base pair in tRNAs. *RNA* 13(9):1427–1436.

63. Taufer M, et al. (2009) PseudoBase++: An extension of PseudoBase for easy searching, formatting and visualization of pseudoknots. *Nucleic Acids Res* 37(Database issue):D127–D135.

64. McCown PJ, Roth A, Breaker RR (2011) An expanded collection and refined consensus model of glmS ribozymes. *RNA* 17(4):728–736.

65. Binkley J, et al. (1995) RNA ligands to human nerve growth factor. *Nucleic Acids Res* 23(16):3198–3205.

66. Fiala R, Munzarová ML, Sklenár V (2004) Experiments for correlating quaternary carbons in RNA bases. *J Biomol NMR* 29(4):477–490.

67. Wöhnert J, Ramachandran R, Görlach M, Brown LR (1999) Triple-resonance experiments for correlation of H5 and exchangeable pyrimidine base hydrogens in (13)C, (15)N-labeled RNA. *J Magn Reson* 139(2):430–433.

68. Cavanagh J, Rance M (1969) Sensitivity improvement in isotropic mixing (TOCSY) experiments. *J Magn Reson* 88(1):72–85.

69. Peterson RD, Theimer CA, Wu H, Feigon J (2004) New applications of 2D filtered/edited NOESY for assignment and structure elucidation of RNA and RNA-protein complexes. *J Biomol NMR* 28(1):59–67.

70. Kim NK, et al. (2008) Solution structure and dynamics of the wild-type pseudoknot of human telomerase RNA. *J Mol Biol* 384(5):1249–1261.

71. Koradi R, Billeter M, Wüthrich K (1996) MOLMOL: A program for display and analysis of macromolecular structures. *J Mol Graph* 14(1):51–55, 29–32.

72. Lavery R, Sklenar H (1989) Defining the structure of irregular nucleic acids: Conventions and principles. *J Biomol Struct Dyn* 6(4):655–667.

73. Staple DW, Butcher SE (2005) Pseudoknots: RNA structures with diverse functions. *PLoS Biol* 3(6):e213.

74. Leontis NB, Westhof E (2001) Geometric nomenclature and classification of RNA base pairs. *RNA* 7(4):499–512.

BIOPHYSICS AND COMPUTATIONAL BIOLOGY